

# Longitude-Resolved Imaging of Jupiter at $\lambda = 2$ cm

R.J. Sault, Chermelle Engel, and Imke de Pater

Australia Telescope National Facility  
CSIRO, Epping, NSW 2121, Australia

Astronomy Department, 601 Campbell Hall  
University of California, Berkeley CA 94720

arXiv:astro-ph/0612769v1 28 Dec 2006

Pages: 28

Tables: 0

Figures: 5

**Proposed Running Head:** Longitude-Resolved Imaging of Jupiter

## **Editorial correspondence to:**

R.J. Sault  
Australia Telescope National Facility  
Locked Bag 194  
NARRABRI, NSW, 2390  
AUSTRALIA Email: rsault@atnf.csiro.au

## Abstract

We present a technique for creating a longitude-resolved image of Jupiter’s thermal radio emission. The technique has been applied to VLA data taken on 25 January 1996 at a wavelength of 2 cm. A comparison with infrared data shows a good correlation between radio hot spots and the 5  $\mu\text{m}$  hot spots seen on IRTF images. The brightest spot on the radio image is most likely the hot spot through which the Galileo probe entered Jupiter’s atmosphere. We derived the ammonia abundance (= volume mixing ratio) in the hot spot, which is  $\sim 3 \times 10^{-5}$ , about half that seen in longitude-averaged images of the NEB, or less than 1/3 of the longitude-averaged ammonia abundance in the EZ. This low ammonia abundance probably extends down to at least the 4 bar level.

## 1. Introduction

### *Radio Astronomy*

Conventional radio interferometry images are integrated over many hours, with 12 or more hours not being unusual. This is required both to meet the required sensitivity and to use Earth rotation synthesis to achieve good sampling of the Fourier plane. Consequently, imaging planets in the conventional way rotationally smears any longitudinal structure. In principle one can merge together snapshots of the same rotational aspect of the planet, from observations taken on different days. This approach was probably first used by de Pater (1980) when observing Jupiter. In practice, the longitudinal smearing is still limited by the fineness of the rotational phase bins that the data are broken into. At decimetric wavelengths, the spatial resolution of the data used to be a significant fraction of a planetary radius, and extra smearing caused by rotation was not so severe. These are typically tens of degrees of rotation. To image the thermal radiation of the planet itself, one requires a higher resolution, typically 1-2'' for Jupiter, or an integration time of less than 10 minutes. Such an image has such poor signal-to-noise that even the North Equatorial Belt (NEB) on Jupiter may not be recognized. To date, all radio wavelength images of Jupiter’s thermal emission have therefore been averaged over longitude (i.e., integrated over hours rather than minutes of time).

Sault *et al.* (1997) developed an alternative technique for Jupiter’s synchrotron emission, based on a three-dimensional tomographic approach. This technique cannot be used for the thermal emission from the disk of a planet. The present paper describes a technique to form a radio “map” of a planet’s thermal radio emission which avoids rotational smearing, but which still allows good sensitivity and Fourier plane sampling. The main motivation to develop this technique has been the need to form radio maps of Jupiter.

### *Jupiter Science*

Infrared observations of Jupiter at 5  $\mu\text{m}$  show that the NEB is not a smooth belt, but rather contains numerous “hot spots” – regions which are much hotter than their surroundings. In these hot spots, one probes relatively deep, hot, levels in Jupiter’s atmosphere because the infrared opacity is relatively low here. A main source of opacity at these wavelengths is cloud layers; i.e., the absence of cloud particles in hot spots lets one probe much deeper layers.

The general consensus therefore has been that hot spots are dry regions on Jupiter, perhaps areas of downdrafts: rising air on the planet cools off, and once the temperature drops below the condensation temperature of ammonia gas, droplets and clouds form. Above the clouds the air is dry, and if there are places of downdrafts the air may indeed be dry and hence devoid of cloud particles.

On 7 December 1995 at 22:10 UT the Galileo probe entered Jupiter’s atmosphere, by chance entering in a hot spot (at a joviocentric latitude of  $6.5^\circ$  N and at  $\sim 4.5^\circ$  West longitude (Syst. III); e.g., Orton *et al.* 1998). During its descent, the probe measured the atmospheric structure (temperature, pressure, density), gas composition and cloud properties down to a depth of  $\sim 20$  bar. Folkner *et al.* (1998) derived the ammonia abundance profile in the hot spot from the gradual and progressive attenuation of the probe signal (at 1.4 GHz) while the probe was descending in Jupiter’s atmosphere. They determined an  $\text{NH}_3$  abundance  $\sim 3.6 \pm 0.5 \times$  the solar N value<sup>[1]</sup> at pressures between 8 and 12 bar, with a possible decrease at higher altitudes. The  $\text{NH}_3$  abundance has since been obtained from the Galileo probe data (Mahaffy *et al.* 1999), and was found to be  $3.2 \pm 1.4 \times$  solar N, i.e., consistent with the results of Folkner *et al.* (1998). Sromovsky *et al.* (1998) deduced an  $\text{NH}_3$  profile at  $P \lesssim 3$  bar from data taken with the Net Flux Radiometer (NFR) on board the Galileo probe. They found that  $\text{NH}_3$  in the hot spot was decreasing linearly from  $0.5 \times$  solar N at 2 bar to  $0.01 \times$  solar at  $P \approx 0.5$  bar. The Galileo probe further measured very low abundances of  $\text{H}_2\text{S}$  at  $P \lesssim 10$  bar and  $\text{H}_2\text{O}$  at  $P \lesssim 20$  bar. Various researchers have investigated downdrafts and planetary waves to explain the altitude profiles of the condensible gases as measured by the Galileo probe (see, e.g., Atreya *et al.* 1996; Showman and Ingersoll 1998; Wong *et al.* 1998; Showman and Dowling 2000; Friedson and Orton 1999).

De Pater *et al.* (2001) (henceforth referred to as dP2001) observed Jupiter at radio wavelengths (at 2, 3.6 and 6 cm wavelength) near the time of the probe entry. Since the main source of opacity at radio wavelengths is ammonia gas, dP2001 derived the disk-averaged ammonia abundance profile from the data and compared this with the Galileo probe results. They could only reconcile an  $\text{NH}_3$  abundance  $\sim 3.6 \pm 0.5 \times$  the solar N value at  $P > 8$  bar if the  $\text{NH}_3$  abundance decreases globally at  $P < 4$  bar, and to subsolar values at pressures  $P \lesssim 2$  bar. They further show (based upon disk-resolved but longitude-averaged images) that the  $\text{NH}_3$  abundance in the NEB is  $\sim 50 - 70\%$  of the value in the EZ (Equatorial Zone), while it is subsolar in both bands at  $P < 2$  bar. In the NEB this low abundance has to extend down to  $P \sim 4 - 6$  bar.

With longitude-resolved radio images one could correlate the occurrence of infrared hot spots with radio hot spots, if they were to exist. Moreover, the main source of opacity at the two wavelength ranges is different: at radio wavelengths one is sensitive to the condensible gas, ammonia, while at IR wavelengths one is sensitive to cloud particles. So

---

<sup>[1]</sup> We use the solar elemental ratios for N, O, and S given in Anders and Grevesse (1989) and for C given in Grevesse *et al.* (1991). The solar N/H value is  $1.12 \times 10^{-4}$ . The volume mixing ratio or mole fraction of solar N in Jupiter’s atmosphere is  $1.97 \times 10^{-4}$ . We use the word abundance as having the same meaning as volume mixing ratio or mole fraction.

microwave observations would provide information on the condensible gas, a necessary piece of information for the development of dynamical models of Jupiter’s atmosphere.

To investigate the occurrence of hot spots, and in particular the hot spot in which the Galileo probe descended, we developed an algorithm to construct a longitude-latitude map of Jupiter, and applied this algorithm to 2-cm data taken at the VLA near the time the Galileo probe descended into Jupiter’s atmosphere; the longitude-averaged maps were presented in dP2001. In this paper we discuss the algorithm (Section 2) and present the observations (Section 3) and results (Section 4).

## 2. The mapping technique

To understand the basis of our mapping technique, consider Fig. 1. Figure 1a shows four identical crosses as they would appear on the face of the planet. The viewing geometry distorts the appearance of the crosses – Fig 1b presents the crosses side-by-side to help accentuate the distortions. On a sufficiently small scale, this distortion can be approximated as a linear transformation of the coordinate system. That is, to first approximation, by appropriate rotation and skew (length scaling), we can convert each of the four crosses into the others. In particular, the appropriate transformation can convert the three right-most crosses to that which would be seen face on.

Applying this to the problem of imaging a rotating planet, all the data (from different viewing aspects) of a sufficiently small facet can be transformed such as they would appear as seen face on. All the data can then be co-added. This assumes that there are no other changes in the emission other than the viewing geometry, e.g. local solar time effects or limb effects are negligible.

In interferometry, where the basic data are samples in the Fourier domain, these manipulations are conveniently done in the Fourier domain. The manipulated visibility data can then be Fourier transformed to form an image of the facet. The details of the manipulations that must be done on the visibilities are described in Appendix A. Briefly, however, they amount to three operations. In imaging a particular facet, the operations that need to be applied to each visibility datum are:

- 1 Apply a phase term to shift the data so that the phase center is the center of the facet. This shift can account for the motion of the facet across the face of the planet.
- 2 Apply a linear transformation to the  $u - v$  coordinates of the data. This corrects for the viewing geometry of the facet as it rotates across the planet. This transformation can readily cope with an oblate spheroid (not just a sphere). A correction for differential rotation can also be made in this step: differential rotation can be modelled as a latitudinal and time dependent stretching in the longitudinal direction which is relevant for the gas giants. The winds on Jupiter are largest near the equator,  $\sim 100$  m/s; since features here move  $\lesssim 3^\circ$  in 10 hours ( $\lesssim 1.3''$  as seen from Earth), we ignored differential rotation.
- 3 Scale up the data (and consequently its noise variance) to account for the change in the projected area. As the facet approaches the limb of the planet, this scale factor approaches infinity, and the signal to noise ratio of the data approaches zero.

Note that the details of each step changes as a function of time (or viewing geometry). The steps can also readily handle changes in the observer-planet distance and geometry during the course of the observation.

When imaging this facet, we weight the visibility data inversely with the noise variance. This gives little weight to data measured near the limb of the planet. Consequently the variance of the resultant image is not particularly degraded by limb data. We further use weighting schemes such as Briggs' robust weighting (1995) to protect against excessively noisy data.

Before visibility manipulation and imaging, it is sensible to subtract a uniform model of the planet, so that we are imaging only deviations from this model. For example, in the data presented below, we have subtracted a model corresponding to a constant temperature oblate spheroid with limb darkening (see Butler and Bastian 1999 for the corresponding visibility function), the best-fit parameters for which were derived from the data.

Mapping a large part of the planet (not a single small facet) can be achieved by stitching together a number of facets. The stitching proceeds by regriding the facets to a common mapping geometry (e.g. Mercator) and feathering them together in any overlap region. In doing this, we are effectively approximating a sphere by a large number of facets.

Note that each facet will have a different Fourier sampling function from the others, and so the point-spread function will vary from facet to facet. This change will be quite large between the planet's pole and equator, and will also be large between different longitudes if only a fraction of a planet's rotation is observed. The map stitched from facets cannot be deconvolved with any conventional technique (these assume a position-independent point-spread function). Although deconvolution can be done before the facets are stitched together, this is not optimal as it cannot deconvolve sidelobes originating from emission in other facets. Making large, overlapping facets will tend to mitigate this, and the changing geometry will tend to smear out distant emission anyway. It will be more of an issue where the Fourier sampling in each facet is poor - this is not the case in the data we present. However a more sophisticated joint algorithm could be expected to give some advantage. For example, an approach similar to that used by Cornwell and Perley (1992) is possible. Their algorithm was one used to deconvolve radio images of the sky when the curvature of the celestial sphere becomes appreciable. They did this by approximating the celestial sphere as a collection of facets. In the results we present below, we have simply deconvolved facets individually.

Because the size of the point-spread function varies between facets, so does the brightness sensitivity. As a map in temperature units is generally more relevant in planetary work, the flux units of the facets have been converted to brightness temperature units before the stitching operation.

An alternative approach to producing a longitude-resolved map of the planet would be to make images of the entire disk at each sampling instant of time, to deconvolve each of these images, regrid them to a common mapping geometry and then to perform a weighted sum. This technique has the advantage that at each time instant, each image is related to the true image by a convolution relationship: a conventional deconvolution algorithm could be used

to remove the effect of a poor Fourier coverage. Note, however, that this approach would be computationally significantly more expensive. However, more importantly, this approach usually fails as a result of two characteristics: that the deconvolution operation in radio interferometry is by necessity a non-linear operation, and such deconvolution algorithms perform poorly when the signal-to-noise in the image is very poor and/or when a complex object is imaged with poor Fourier sampling. Unfortunately the image formed from a single time instant will have poor sensitivity and poor Fourier coverage. Our approach avoids these pitfalls by performing the geometric manipulations before the deconvolution step: each facet is a result of all available visibility data.

### 3. Observations and Data Analysis

As detailed in dP2001, in order to ‘mark’ the location of the Galileo probe entry on a radio image, we observed the planet with the VLA as close to the probe entry time as possible. Unfortunately, when the probe entered Jupiter’s atmosphere on December 7, 1995, the planet was close to conjunction (Dec. 19, 1995) and the array was in the B-configuration, so that much of Jupiter’s emission would be significantly resolved out at short wavelengths. So this period was less than ideal to image Jupiter’s thermal emission. Observers at optical and infrared wavelengths also could not observe the planet with high spatial resolution because of its close proximity to the Sun. Therefore, IRTF (InfraRed Telescope Facility) images taken by Orton *et al.* (1998) and Ortiz *et al.* (1998) to determine the probe entry point in relation to infrared hot spots were taken on and before 21 November 1995 and started again on 22 January 1996. From the long (many years) time series of images Orton *et al.* and Ortiz *et al.* determined the most likely appearance of the probe’s entry site, or hot spot through which it entered on Dec. 7 through an interpolation and extrapolation of their data. After applying a drift correction rate of 103.5 m/s for the period March – December 1995 and of 102.5 m/s from January – May 1996, features at the latitude of the probe entry site were visible at the same location (in System III coordinates) in all their images. The infrared intensity, and hence possible dryness, and the shape of the hot spot varied considerably, however, on timescales of weeks.

On January 25, approximately 1.5 months after the probe’s descent when the VLA had partially moved to the more compact C-configuration, we observed the planet at a wavelength of 2 cm. The resolution (FWHM) in this configuration is  $\sim 1 - 1.5''$ , and the array was sensitive to structures up to  $\sim 90''$ . At this wavelength Jupiter’s synchrotron radiation is very low compared to its thermal emission ( $\lesssim 3\%$ ; Bolton *et al.* 2002; de Pater and Dunn, 2003), and one probes below the ammonia-ice clouds, which makes observations at this wavelength ideal for imaging the planet’s thermal emission. We observed the planet for a total of  $\sim 6 - 7$  hours. As mentioned in Section 2, we first constructed a model of a uniform oblate spheroid which best matched the data; this model was subtracted from the data before we applied the imaging technique. This model is very similar to that determined in dP2001: the disk-averaged temperature is 150 K (the uncertainty is about 5 K), and limb darkening parameter  $p = 0.05$ , where limb darkening is parameterized as:  $I_0 \cos^p(\theta)$ , with  $I_0$  the brightness temperature and  $\theta$  the angle between the line of sight and the normal to the surface (Butler and Bastian, 1999).

As described in Section 2 and the Appendix, we imaged facets on Jupiter every 10 degrees in latitude and longitude. Each facet was  $60^\circ$  in size on Jupiter. Each facet was deconvolved using a CLEAN algorithm (Högbom 1974) and the intensity units expressed in brightness temperature, using the appropriate resolution of that facet to convert from Jy to Kelvin. The facets were then stitched together: the resulting map is shown in Fig. 2. Since our observing run did not cover Jupiter’s full rotation, the map does not extend over the full  $360^\circ$  in longitude. Fig. 3 shows a similar map of the point-spread functions; this gives the reader an idea of the change in point-spread function size as it varies with location on the map.

#### 4. Discussion

##### *Comparison with IRTF data*

The resemblance of our radio map (Fig. 2) with infrared images as presented by Orton *et al.* (1998) and Ortiz *et al.* (1998) is striking. Series of hot spots show up at jovigraphic latitudes between  $7 - 11^\circ$ , i.e., in the same latitude band as the hot spots seen at infrared wavelengths. The bright spot at a West longitude of  $19.7^\circ$  (Sys. III), and jovigraphic latitude  $9.5^\circ$  N (= jovicentric latitude of  $8.3^\circ$  N) is most likely the hot spot through which the Galileo probe entered; henceforth referred to as the ‘Galileo’ hot spot. Orton *et al.* (1998) and Ortiz *et al.* (1998) showed that the spots in this latitude range typically move at a rate between 99 and 105 m/s in the prograde direction. If the average wind velocity between Dec. 7 1995 and Jan. 25 1996 was 101.5 m/s, the hot spot through which the Galileo probe entered would have been exactly at the longitude we see the brightest spot in our map. Orton *et al.* (1998) show that a drift rate of 103 m/s does best match the IRTF observations between November 1995 and January 1996. Fig. 4 shows a comparison of the NEB as presented in Fig. 2 (bottom figure) with IRTF data from Ortiz *et al.* (1998) (top figure). The IRTF image was taken on 22 January 1996, at a central meridian longitude  $\lambda_{III} = 21^\circ$ . We deprojected the IRTF image onto a grid similar in size to the grid of the radio image. At a drift rate of 103 m/s, features in this latitude band should have moved  $20.6^\circ$  between the time the IRTF image was taken (22 Jan. 1996 at  $\sim 19:35$  UT) and the midpoint of the radio image (25 Jan. 1996 at  $\sim 16:30$  UT). The features in the two images are thus lined up with respect to each other, assuming a 103 m/s wind velocity. As shown, each infrared hot spot within  $\sim 45^\circ$  from the center shows up as a radio hot spot. We see a few more radio hot spots at larger distances from the center, which would put the infrared counterparts too close to the limb on the infrared image for proper deprojection.

A comparison of the images in Figure 4 clearly shows that the infrared hot spots are also hot spots at radio wavelengths. The main source of opacity at infrared wavelengths are cloud particles: hot spots are known to be devoid of clouds. At radio wavelengths the main source of opacity is ammonia gas. Because the brightness temperature in the hot spots is much larger than in surrounding regions, the ammonia gas abundance must be less so that deeper warmer layers in Jupiter’s atmosphere are probed. Since ammonia gas is the condensible gas in Jupiter’s upper troposphere, we say, in analogy to Earth’s atmosphere, that hot spots on Jupiter apparently contain ‘dry air’. In the following section we will

derive the ammonia abundance in the Galileo hot spot, and compare this with the overall ammonia abundance in the NEB and EZ.

### *Ammonia Abundance*

The brightness temperature in the Galileo hot spot is  $\sim 170$  K, or  $\sim 20$  K above the general background, and  $\sim 25$  K hotter than the Equatorial Zone. Below we will work with differences in brightness temperature rather than the absolute values, since missing short spacings in the data tend to decrease the overall brightness temperature. dP2001 performed calculations to derive the most plausible longitude-averaged  $\text{NH}_3$  abundance profile in the NEB and EZ, based upon observations at 2, 3.6 and 6.2 cm. They concluded that the  $\text{NH}_3$  abundance in the NEB is roughly  $6 \times 10^{-5}$  down to pressure levels of  $\sim 6$  bar, with an  $\text{NH}_3$  abundance in the EZ of  $\sim 1 \times 10^{-4}$  at  $P < 4$  bar; the  $\text{NH}_3$  increases at larger depths as measured by the Galileo probe. With a temperature difference between the hot spot and the EZ of  $\sim 25$  K at 2 cm, the  $\text{NH}_3$  abundance in the hot spot must be approximately half that in the NEB, or  $\sim 3 \times 10^{-5}$ , down to  $P > 4$  bar. Since we do not have longitude-resolved images at longer wavelengths we cannot determine the depth down to which this low  $\text{NH}_3$  abundance does extend.

NFR data from the Galileo probe have been analyzed by Sromovsky *et al.* (1998), and their derived ammonia profile is shown in Fig. 5 (dashed line). Since the probe entered the hot spot, this profile should be appropriate for the hot spot at the time of probe entry. We further indicated on this figure the hot spot profile as measured with the Infrared Space Observatory (ISO; Fouchet *et al.* 2000a). The latter profile is also quite similar to that presented by Fouchet *et al.* (2000b) based upon  $5 \mu\text{m}$  FTS data taken with the Canada-France-Hawaii telescope (CFHT). The general figure and the weighting functions at the various radio wavelengths were taken from dP2001.

We have tried to match the radio data with the NFR ammonia profile, but have not succeeded. In order to match the disk-averaged brightness temperature at 2–6 cm wavelength, the global ammonia abundance cannot be above  $\sim 1 \times 10^{-4}$  at  $P < 2 - 3$  bar. Since the EZ is not a particularly cold region at radio wavelengths, the  $\text{NH}_3$  abundance in the EZ cannot be over  $1 \times 10^{-4}$ . This profile is indicated on Fig. 5. At larger depths we adopted the ammonia profile as measured by the Galileo probe (Folkner *et al.* 1998). As already mentioned in dP2001, the ammonia abundance in the NEB should be  $\sim 6 \times 10^{-5}$  down to a depth of 5–6 bars. This profile is also indicated on Fig. 5. To match the Galileo hot spot temperature at a wavelength of 2 cm, the ammonia abundance needs to be decreased further to  $3 \times 10^{-5}$ . Due to a lack of longitude resolved images at 3.6 and 6 cm we cannot determine the depth down to which this low  $\text{NH}_3$  abundance extends; based upon the 2 cm data alone we know that it must extend down to at least the 4 bar pressure level. This profile is also indicated on Fig. 5. It does match the ISO profile at pressure levels  $P < 2$  bar extremely well, but our derived  $\text{NH}_3$  abundance at pressures between 2 and 4 bar is typically lower than indicated by the ISO and NFR data. This region is best probed at radio wavelengths of 3 – 6 cm.



## 4. Conclusions

We have presented the first longitude-resolved map of Jupiter’s thermal radio emission at a wavelength of 2 cm. This map clearly shows the presence of radio-bright hot spots. A comparison with IRTF images shows that each radio hot spot is also a hot spot at infrared wavelengths. Hence the hot spots must indeed lack clouds (infrared wavelengths) and the air must be dry (low  $\text{NH}_3$  abundance). We derived an ammonia abundance in the hot spot where the probe went down of approximately  $3 \times 10^{-5}$  down to at least the 4 bar level; we need measurements at longer wavelengths to determine how deep it extends. This abundance is about half the value derived for the NEB, and three times less than that in the EZ, as derived from longitude-averaged images at 2, 3.6 and 6 cm wavelength by dP2001. Our findings agree at pressures  $P \lesssim 2$  bar with the infrared observations of Fouchet *et al.* (2000a, b). However, at pressures between 2 and 4 bar our derived  $\text{NH}_3$  profile in the hot spot is less than the values suggested by Fouchet *et al.* from infrared observations, and also less than the  $\text{NH}_3$  abundance derived by Sromovsky *et al.* (1998) from Galileo’s NFR experiment.

It is desirable to obtain longitude-resolved images of Jupiter at wavelengths of 3.6 and 6 cm. Unfortunately, the 3.6 and 6 cm data presented by dP2001 were snapshots taken on different days. Differential rotation will tend to smear out features if differential rotation is not taken into account. A more difficult problem, however, is Jupiter’s synchrotron radiation, which, relative to the thermal radiation, increases dramatically towards the longer wavelengths. We have therefore not attempted to apply this technique to longer wavelength data.

## Appendix A: Geometry

To image a facet, we would like a set of visibilities that views the facet face on. Instead the visibility data generally corresponds to an oblique view. Our aim then is to correct the visibilities for this distorted view before imaging. In this way, each visibility can potentially contribute to a facet. This appendix addresses two aspects: the distortion produced by the viewing geometry, and how we can account for this distortion in the visibility data before imaging.

As an example of the effect of viewing geometry, consider a cross lying on the surface of a sphere. Figure 1a shows four identical crosses on a sphere, whose appearance is different because of the viewing geometry. Figure 1b shows the same four crosses side by side to accentuate the differences. Provided they are sufficiently small, the difference between the cross viewed face on and the other three crosses can be approximated as a linear distortion and translation in the coordinate system. The distorted coordinates of the cross,  $\mathbf{x}'$  are related to the “face-on” coordinates,  $\mathbf{x}$  as

$$\begin{pmatrix} x' \\ y' \end{pmatrix} = \mathbf{D} \begin{pmatrix} x \\ y \end{pmatrix} + \begin{pmatrix} x_0 \\ y_0 \end{pmatrix}, \tag{1}$$

were  $\mathbf{D}$  is a  $2 \times 2$  matrix. To determine  $\mathbf{D}$ , we compute the appropriate transformation in three-dimensional space that represents the change in the viewing geometry, and then project this onto our two-dimensional view.

Consider a facet centered on the origin in the  $x$ - $y$  plane, which corresponds to a face-on view of a region around the point on Jupiter's surface at longitude, latitude and radius of  $(\lambda_J, \phi_J, r)$ . Assume the sub-Earth point at the time of interest is  $(\lambda_E, \phi_E)$ . We use a Cartesian coordinate system with the  $x$ -axis lying in the equatorial plane, the  $y$ -axis pointing to the pole, and the  $z$ -axis pointing towards the observer. Six transformations are needed to take a facet centered at the origin to the place on Jupiter as dictated by our viewing geometry. These are:

1. Distort by a shearing operation,  $\mathbf{S}$ , to account for differential rotation:

$$S = \begin{pmatrix} 1 & s & 0 \\ 0 & 1 & 0 \\ 0 & 0 & 1 \end{pmatrix}. \quad (2)$$

The skew parameter,  $s$  will depend on the differential rotation rate at different latitudes and the elapsed time from the time of interest to some reference time.

2. Rotate the facet around the  $x$ -axis by an angle,  $\Delta\phi_J$ , which is equal to the difference of the jovigraphic and jovicentric latitude of the facet center. This tilting operation causes the facet to lie tangential to the surface of the planet after subsequent transformations. We label this rotation  $\mathbf{R}_1 = \mathbf{R}_x(\Delta\phi_J)$ .

3. Shift the center of the facet in the direction of the observer so as to make the origin correspond to the center of the planet.

$$\mathbf{r} = \begin{pmatrix} 0 \\ 0 \\ r \end{pmatrix}. \quad (3)$$

Note, as Jupiter is oblate,  $r$  is a function of the latitude of the facet center.

4. Rotate about the  $x$ -axis by the the jovicentric latitude,  $\phi_J$  (i.e. rotate the feature to the correct latitude). Represent this by  $\mathbf{R}_2 = \mathbf{R}_x(\phi_J)$ .

5. Rotate about the  $y$ -axis by the difference between the longitude of interest and the sub-Earth longitude. This rotates the feature to the correct longitudinal view. Represent this by  $\mathbf{R}_3 = \mathbf{R}_y(\lambda_J - \lambda_E)$ .

6. Rotate about the  $x$ -axis by an angle being the negative of the (jovicentric) sub-Earth latitude. Represent this by  $\mathbf{R}_4 = \mathbf{R}_x(-\phi_E)$

The overall transformation is

$$\mathbf{x}' = \mathbf{R}_4 \mathbf{R}_3 \mathbf{R}_2 \mathbf{R}_1 \mathbf{S} \mathbf{x} + \mathbf{R}_4 \mathbf{R}_3 \mathbf{R}_2 \mathbf{r} \quad (4)$$

Ultimately we are interested only in the projection on the plane of the sky, as indicated in eq. 1. The distortion matrix of interest to us,  $\mathbf{D}$  is the upper-left  $2 \times 2$  sub-matrix of  $\mathbf{R}_4 \mathbf{R}_3 \mathbf{R}_2 \mathbf{R}_1 \mathbf{S}$ . Similarly, our offset  $(x_0, y_0)^T$  is the  $x$  and  $y$  component of  $\mathbf{R}_4 \mathbf{R}_3 \mathbf{R}_2 \mathbf{r}$ .

Given the image plane transformation that models the viewing geometry, we can determine the effect on the visibility by using the following Fourier theorem:

For a Fourier pair,

$$f(\mathbf{x}) \Leftrightarrow F(\mathbf{u}), \quad (5)$$

and a linear transformation of the coordinate system

$$\mathbf{x}' = \mathbf{D}\mathbf{x}, \quad (6)$$

then the following is a Fourier transform pair

$$f(\mathbf{D}^{-1}\mathbf{x}') \Leftrightarrow \det(\mathbf{D})F(\mathbf{D}^T\mathbf{u}'). \quad (7)$$

where  $\mathbf{u}'$  is the Fourier transform coordinates corresponding to  $\mathbf{x}'$ .

In our situation, we measure visibilities in the distorted frame, i.e. what we measure is  $\det(\mathbf{D})F(\mathbf{D}^T\mathbf{u}')$ . Consequently, correcting the viewing distortion in the visibilities consists of producing ‘corrected’ Fourier coordinates,

$$\begin{pmatrix} u \\ v \end{pmatrix} = \mathbf{D}^T \begin{pmatrix} u' \\ v' \end{pmatrix}, \quad (8)$$

and dividing the correlations (and the recorded rms noise) by  $\det(D)$ . The correlations also have to be phase rotated, to account for the shift of  $(x_0, y_0)^T$ .

The determinant,  $\det(D)$ , is related to the change in projected area of the facet when viewed obliquely. For a feature approaching the limb of the planet, the projected area approaches zero, and hence dividing by the determinant amplifies the noise level. When a feature is behind the planet, the projected area becomes negative. We have arbitrarily discarded visibilities when the determinant drops below 0.1 (i.e. an incident angle of  $84^\circ$ ). Additionally, in the imaging step, we have weighted visibility data by the reciprocal of the noise variance. In doing this, we weight down visibility data corresponding to when a feature is near the limb of the planet.

### *Acknowledgements*

We thank Glenn Orton and Jose Ortiz for providing us with the IRTF image, a portion of which is shown in Fig. 4. This research has in part been funded by NASA grant NAG5-12062 to the University of California in Berkeley.

## References

- Anders, E., and N. Grevesse, 1989, Abundances of the elements: meteoritic and solar, *Geochimica et Cosmochimica Acta* Vol. **53**, 197-214
- Atreya, S.K., T. Owen, and M. Wong, 1996. Condensible Volatiles, Clouds, and Implications for Meteorology in the Galileo Probe Entry Region: Jupiter Is Not Dry!. *BAAS* **28**, 1133.
- Bolton, S. J. and 20 additional authors, 2002. Ultra-relativistic electrons in Jupiter's radiation belts. *Nature* **415**, 987-991
- Briggs, D., 1995, High fidelity deconvolution of moderately resolved sources, PhD Thesis, New Mexico Institute of Mining and Technology, Socorro NM (<http://www.aoc.nrao.edu/ftp/dissertations/dbtriggs/diss.html>)
- Butler, B.J. and T.S. Bastian, 1999. Solar system objects. *Synthesis Imaging in Radio Astronomy II, ASP Conference series* **180**. Eds. G.B. Taylor, C.L. Carilli, and R.A. Perley.
- Cornwell, T.J., and R.A. Perley, 1992. Radio-interferometric imaging of very large fields – The problem of non-coplanar arrays. *Astron. Astrophys.* **261**, 353-364.
- de Pater, I., 1980. 21 cm maps of Jupiter's radiation belts from all rotational aspects, *Astron. Astrophys.* **88**, 175-183.
- de Pater, I. and D.E. Dunn, 2003. VLA Observations of Jupiter's Synchrotron Radiation at 15 and 22 GHz. *Icarus* **163**, 449-455.
- de Pater, I., D. Dunn, K. Zahnle and P.N. Romani, 2001. Comparison of Galileo Probe Data with Ground-based Radio Measurements. *Icarus*, **149**, 66-78 (dP2001)
- Folkner, W.M., R. Woo, and S. Nandi, 1998. Ammonia abundance in Jupiter's atmosphere derived from the attenuation of the Galileo probe's radio signal. *J. Geophys. Res. Planets*, **103**, 22847-22856.
- Fouchet, T., E. Lellouch, B. Bezard, T. Encrenaz, and P. Drossart, 2000. ISO-SWS observations of Jupiter: measurement of the ammonia tropospheric profile and of the  $^{15}\text{N}/^{14}\text{N}$  isotopic ratio. *Icarus* **143**, 223-243.
- Fouchet, T., E. Lellouch, J.-P. Maillard, B. Bezard, C. Cottaz, and I. Kleiner, 2000. Determination of Jupiter's N/H ratio from FTS observations at 5 micron. *BAAS* **32**, # 12.16
- Friedson, A.J. and G.S. Orton, 1999. A dynamical model of Jupiter's 5-micron hot spot. *BAAS* **31**, 1155.
- Grevesse, N., D.L. Lambert, A.J. Sauval, E.F. van Dishoeck, C.B. Farmer, and R.H. Norton, 1991, Vibration rotation bands of CH in the solar infrared spectrum and the solar carbon abundance, *Astron. Astrophys.* **242**, 482-495.

- Högbom, J.A., 1974, Aperture synthesis with a non-regular distribution of interferometer baselines, *Astron. Astrophys*, **15**, 417-426. Mahaffy, P.R., H.B. Niemann, and J.E. Demick, 1999. Deep Atmosphere Ammonia Mixing Ratio at Jupiter from the Galileo Probe Mass Spectrometer. *BAAS* **31**, 5205.
- Ortiz, J.L., G.S. Orton, A.J. Friedson, S.T. Stewart, B.M. Fisher, and J.R. Spencer, 1998, Evolution and persistence of 5- $\mu$ m hot spots at the Galileo probe entry latitude. *J. Geophys. Res.* **103**, 23,051-23,069.
- G.S. Orton, B.M. Fisher, K.H. Baines, S.T. Stewart, A.J. Friedson, J.L. Ortiz, M. Marinova, M. Ressler, A. Dayal, W. Hoffmann, J. Hora, S. Hinkley, V. Krishnan, M. Masanovic, J. Tesic, A. Tziolas, and K.C. Parija, 1998. Characteristics of the Galileo Probe entry site from Earth-based remote sensing observations. *J. Geophys. Res.* **103**, 22791–22814.
- Sault, R.J., T. Oosterloo, G.A. Dulk, and Y. Leblanc, 1997, The first three-dimensional reconstruction of a celestial object at radio wavelengths: Jupiter’s radiation belts, *Astron. Astrophys*, **324**, 1190-1196.
- Showman, A.P. and T.E. Dowling 2000. Nonlinear simulations of Jupiter’s 5-micron hot spots. *Science* **289**, 1737-1740.
- Showman, A. P. and A.P. Ingersoll, 1998. Interpretation of Galileo Probe Data and Implications for Jupiter’s Dry Downdrafts. *Icarus* **132**, 205-220.
- Sromovsky, L.A., A.D. Collard, P.M. Fry, G.S. Orton, M.T. Lemmon, M.G. Tomasko, and R.S. Freedman, 1999. Galileo Probe measurements of thermal and solar radiation fluxes in the jovian atmosphere. *J. Geophys. Res.* **103**, 22929–22978.
- Wong, M.H., S.K. Atreya, and P.N. Romani, 1998. Entrainment in the Galileo Probe Site Downdraft. *BAAS*, **30**, 1075.

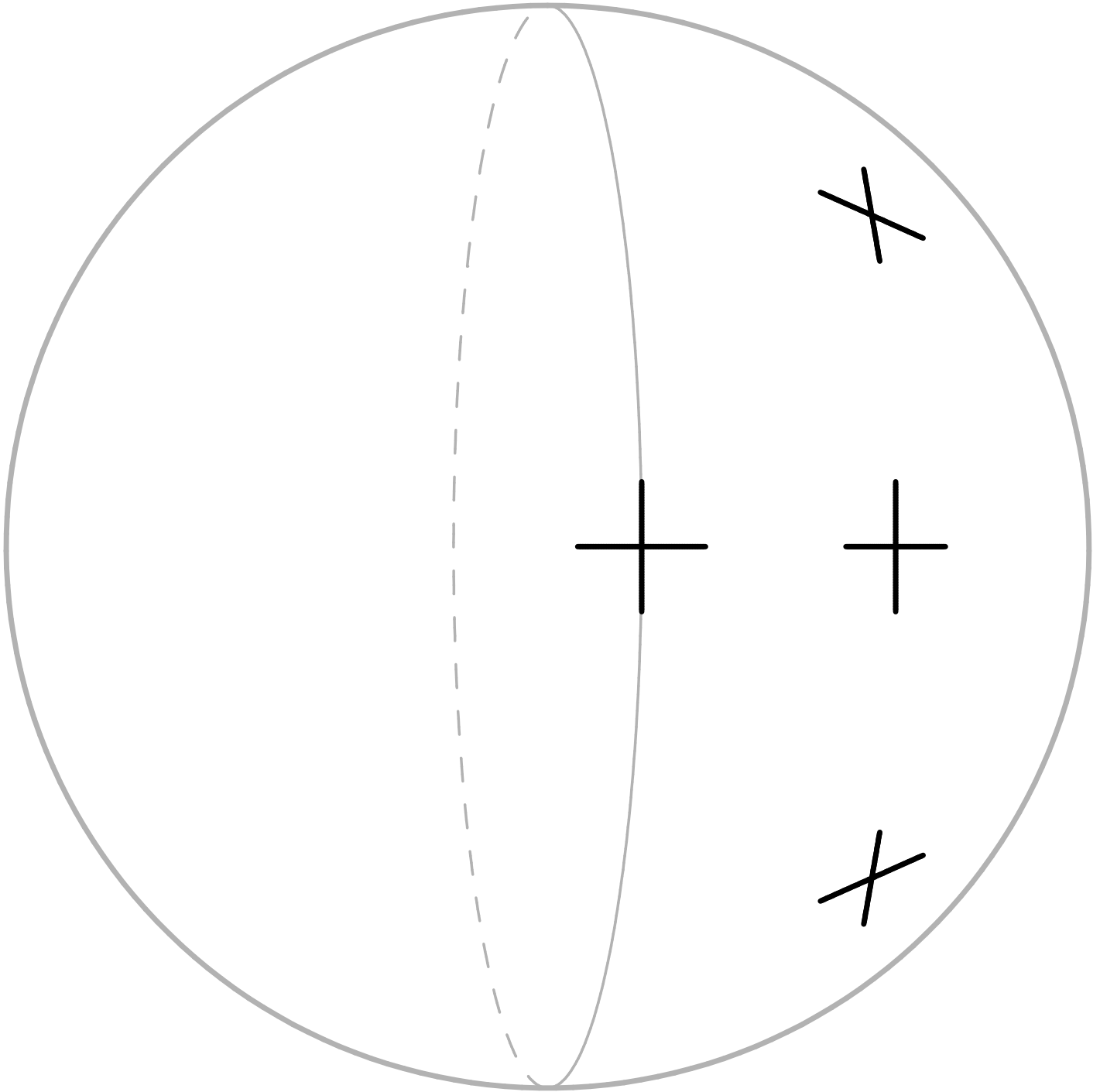




Fig. 1. Four identical crosses on the face of a planet. The viewing geometry distorts the appearance of the crosses – Fig 1b presents the crosses side-by-side to help accentuate the distortions.

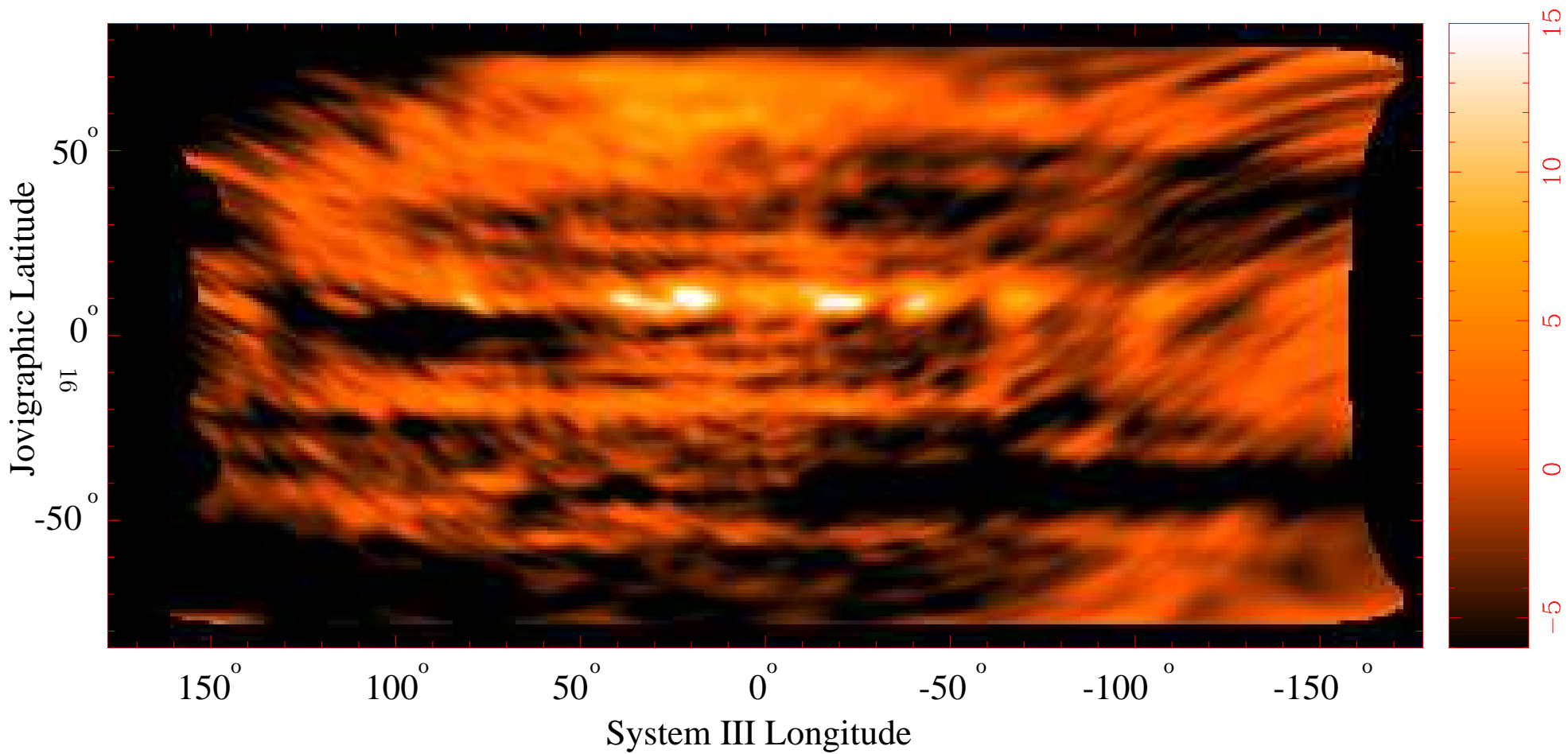




Fig. 2. Radio map of Jupiter at a wavelength of 2 cm. The data were obtained with the VLA on 25 January 1996, and processed as described in this paper. Note that a uniform disk was subtracted, so only deviations in temperature from a 150 K disk are shown.

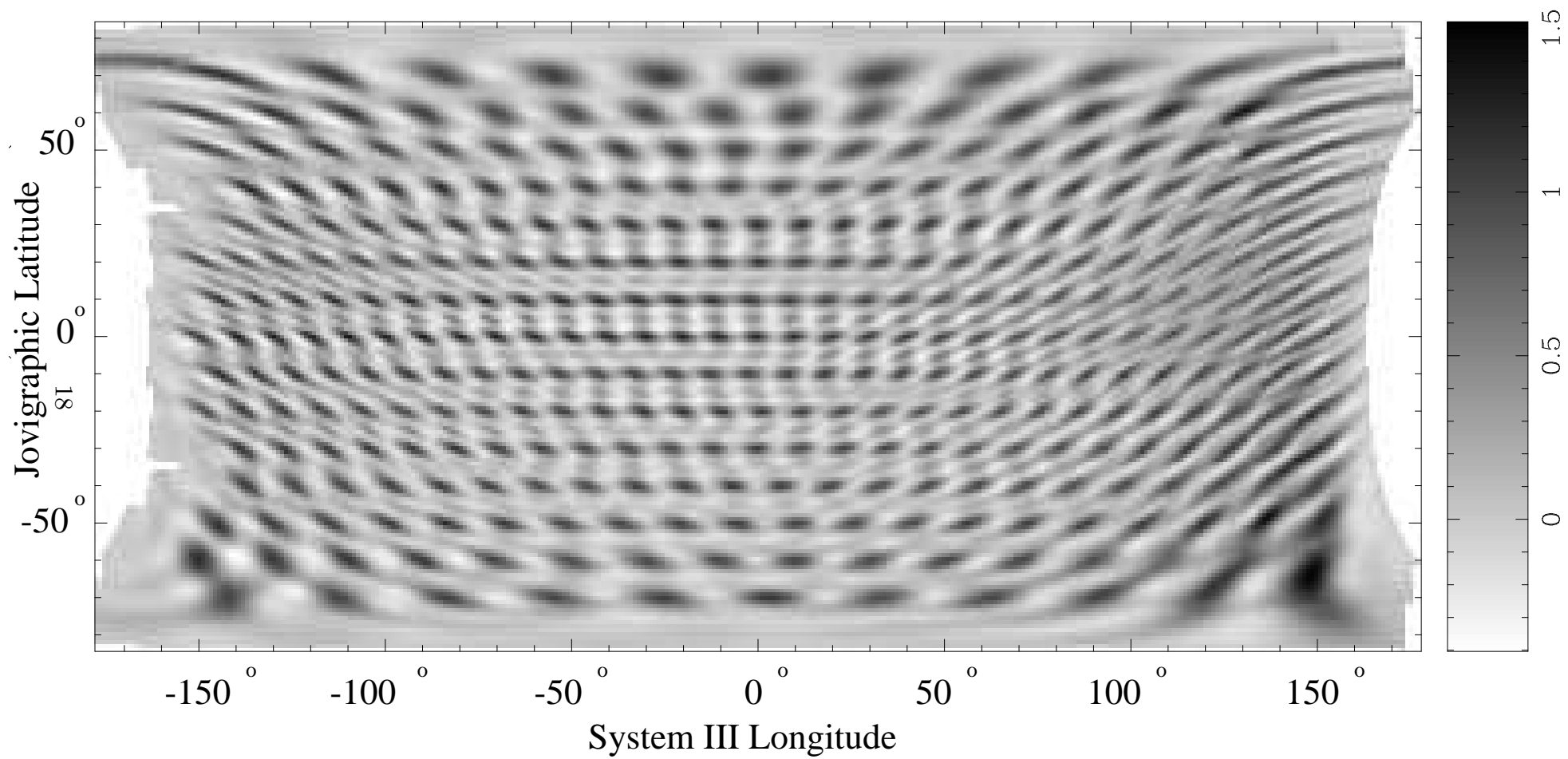


Fig. 3. A representation of the point-spread functions for each facet imaged on the planet.

20

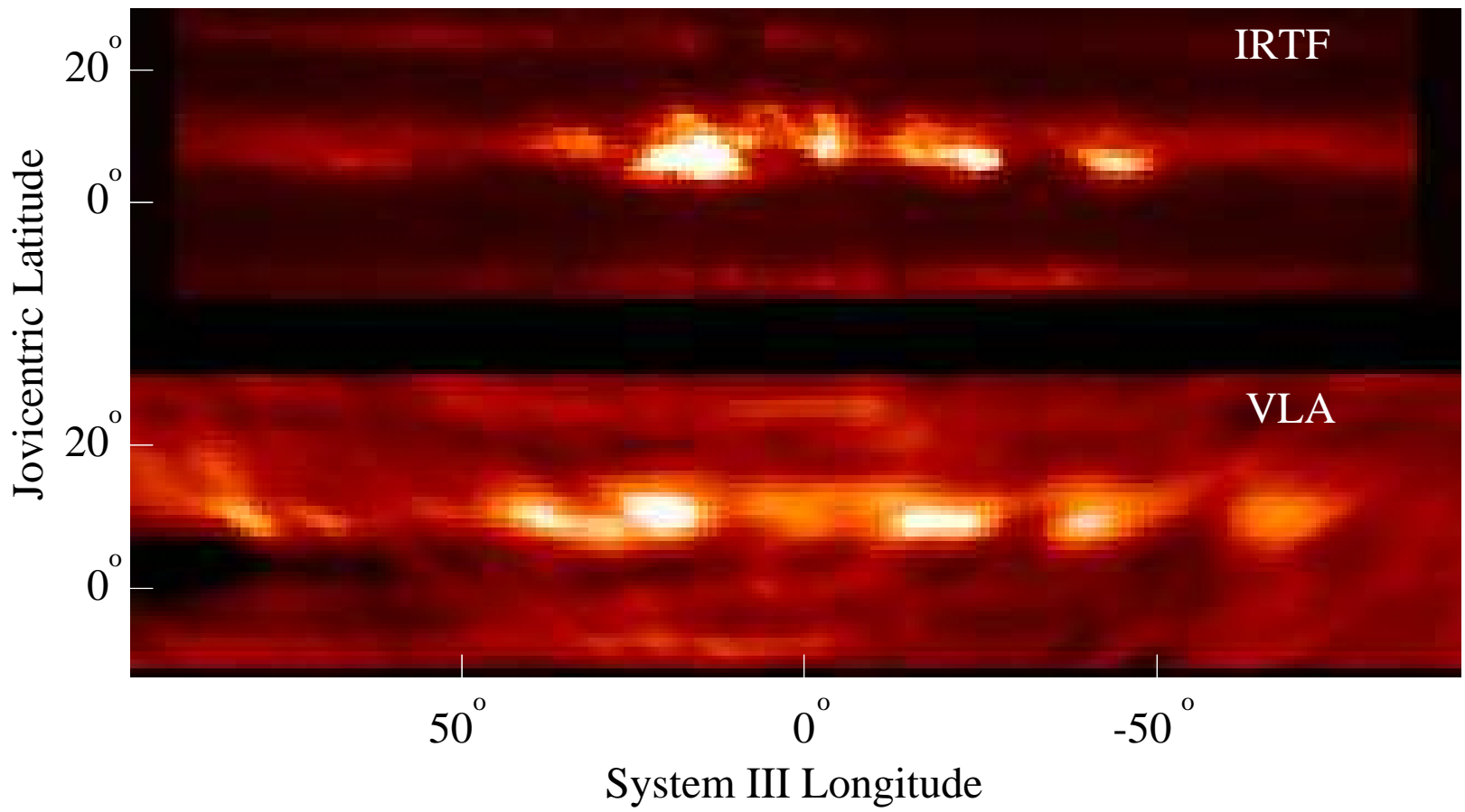


Fig. 4. Comparison of an IRTF image (top) with our radio image (bottom). We show a  $\sim 45^\circ$  latitude range around the NEB on both images (indicated in approximate jovian coordinates), and a  $180^\circ$  view in longitude (in System III coordinates). The IRTF image was taken on 22 January 1996 by J.L. Ortiz and G.S. Orton (see Ortiz *et al.* 1998 and Orton *et al.* 1998). The central meridian longitude in the IRTF image  $\lambda_{III} = 21^\circ$ . With a wind velocity of 103 m/s, the features in the two images line up well.

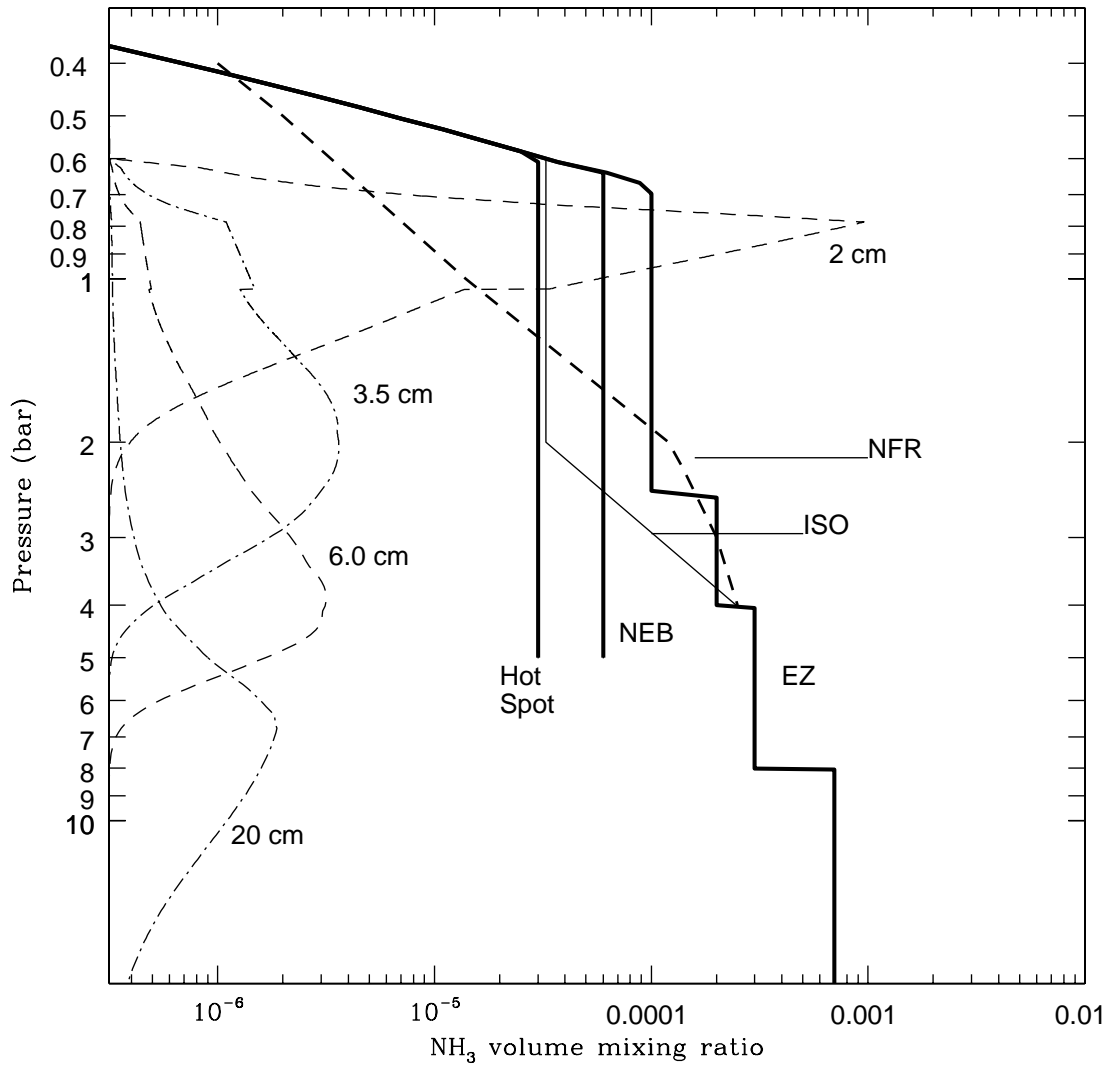


Fig. 5. Graph of the ammonia abundance profiles as derived from the radio data in the EZ, NEB, and Galileo hot spot (see text for detailed explanations). The profile as derived from the NFR data is indicated by the dashed line, and that obtained with ISO by the thin solid line. Weighting functions for the different wavelengths are indicated on the left of the figure (adapted from dP2001).